



Analysing the impact of non-parallelism in Fabry-Perot etalons through optical modelling

DYLAN M. MARQUES,^{1,*}  JAMES A. GUGGENHEIM,^{1,2,3}  AND PETER R. T. MUNRO¹ 

¹*Department of Medical Physics and Biomedical Engineering, University College London, London, UK*

²*Institute of Cardiovascular Sciences, University of Birmingham, Birmingham, UK*

³*School of Computer Science, University of Birmingham, Birmingham, UK*

**dylan.marques.17@ucl.ac.uk*

Abstract: Fabry-Perot (FP) etalons, composed of two parallel mirrors, are used widely as optical filters and sensors. In certain applications, however, such as when FP etalons with polymer cavities are used to detect ultrasound, the mirrors may not be perfectly parallel due to manufacturing limitations. As little is known about how the mirrors being non-parallel impacts upon FP etalon performance, it is challenging to optimize the design of such devices. To address this challenge, we developed a model of light propagation in non-parallel FP etalons. The model is valid for arbitrary monochromatic beams and calculates both the reflected and transmitted beams, assuming full-wave description of light. Wavelength resolved transmissivity simulations were computed to predict the effect that non-parallel mirrors have on the sensitivity, spectral bandwidth and peak transmissivity of FP etalons. Theoretical predictions show that the impact of the non-parallel mirrors increases with both mirror reflectivity and incident Gaussian beam waist. Guidelines regarding the maximum angle allowed between FP mirrors whilst maintaining the sensitivity and peak transmissivity of a parallel mirror FP etalon are provided as a function of mirror reflectivity, cavity thickness and Gaussian beam waist. This information, and the model, could be useful for guiding the design of FP etalons suffering a known degree of non-parallelism, for example, to optimize the sensitivity of polymer based FP ultrasound sensors.

© 2021 Optical Society of America under the terms of the [OSA Open Access Publishing Agreement](#)

1. Introduction

Ideal Fabry-Perot (FP) etalons are composed of two parallel mirrors which form an optical cavity [1]. At most optical wavelengths, an FP etalon is reflective. However, the FP etalon becomes transparent when the optical thickness of the cavity matches an integer number of wavelengths [2]. If designed with parallel and highly reflective mirrors, FP etalons are transparent only within a very narrow spectral band and thus operate as a wavelength filter [3]. Since the central wavelength of the transmitted band, typically called resonance wavelength, changes with the optical cavity thickness, FP etalons can also be used as sensors. A perturbation, such as a pressure wave, modulates the cavity thickness and therefore, indirectly, it modulates the reflectivity and transmissivity of the FP etalon near the resonance wavelength [4].

The optical response of an FP etalon is generally characterized by a spectrally resolved transmissivity or reflectivity measurement typically known as the Interferometer Transfer Function (ITF). The ITF characterizes the performance of an FP etalon as a filter and allows for parameters such as the spectral bandwidth and peak transmissivity to be defined. If an FP etalon is used as a sensor, its optical sensitivity (generally assumed to be proportional to the minimum detectable change in cavity thickness) is related to the maximum derivative of the ITF with respect to wavelength. In general, ITFs from FP etalons with parallel mirrors have higher peak transmissivity, narrower spectral transmission bandwidth and higher sensitivity compared to FP etalons with non-parallel mirrors [5].

Non-parallel FP etalons generally occur due to manufacturing limitations, rather than by design. For example, FP ultrasound sensors employ a polymer cavity [6] to provide a higher compressibility to ultrasound waves compared to traditional FP glass cavities [7]. In this application, due to the challenge of forming a uniform polymer layer, the cavity thickness varies gradually across the surface of the sensor resulting in the FP mirrors being non-parallel [8]. Optimizing the design of non-parallel FP etalons has been challenging up until now, because the impact of non-parallelism on the ITF was not understood. This task is even more challenging since the impact of non-parallelism is expected to vary as a function of mirror reflectivity, cavity thickness and illumination Gaussian beam waist. Understanding the interplay between these design parameters and the non-parallelism is crucial for an efficient optimization of the FP design.

Optical models of non-parallel FP etalon can be used to study the impact of the non-parallelism. Light propagation in non-parallel FP etalons has been studied previously. Xia *et al.* developed a model of Gaussian beam transmission through non-parallel FP etalons by using the theory of Gaussian beam propagation [9]. Xia *et al.* studied the spatial profile of the transmitted beam and the impact of the angle between mirrors on the ITF, for two different mirror reflectivities. This model has the advantage of being fast to compute but is limited to modelling aberration free Gaussian beams. Another model of light propagation in non-parallel FP etalons was developed by Lee *et al.* [5], who created a model based on a combination of angular spectrum propagation, spatial field representation and geometrical optics. The model was used to compute the effect of the angle between mirrors on the ITF from a single FP design. This model has the advantage of being valid for arbitrary incident beams, but requires the evaluation of a two-dimensional Fourier transform to switch between angular spectrum and spatial field representations, for each simulated light round trip inside the cavity. This model is thus computationally expensive, especially for high mirror reflectivities, where the number of round trips necessary for the model to converge increases. We also note that all previously developed models approximate the FP mirrors as ideal, infinitely thin, reflective interfaces.

To provide information about the impact of non-parallelism in the ITF as the design parameters vary a large number of simulations are needed. Therefore, the computational time is an important consideration about the model chosen to perform the simulations. Furthermore, we want our model to be valid for non-Gaussian beams to allow simulation of other beam shapes used in the field, such as Bessel beams [10]. Since no previous models match both specifications we have developed a new model. The new model developed considers an incident angular spectrum and iteratively evaluates the light reflected back and forth between the FP mirrors, using reference frame transformations to take into account the angle between the FP mirrors. The field is always described as an angular spectrum and therefore no two-dimensional Fourier transforms are evaluated in the iterative stage of the algorithm. This significantly reduces the computation time of our model compared to that of Lee *et al.*. By using an angular spectrum description, the model remains valid for arbitrary incident beams, and the mirrors may be described based on their layered refractive index distribution and thickness, or as idealised interfaces with a specified reflectivity. Our model was validated against a model of parallel FP etalon and an alternative, but computationally intensive, non-parallel FP etalon model. The model was used to quantify the impact that non-parallel mirrors have on the ITF as mirror reflectivity, cavity thickness and the Gaussian beam waist vary. Finally, guidelines about the maximum angle between the FP mirrors which can be tolerated, whilst still achieving high peak transmissivity and sensitivity, are presented, also as a function of mirror reflectivity, cavity thickness and the Gaussian beam waist.

2. Theory

We consider a non-parallel FP etalon composed of two mirrors placed in series in their respective reference frames $r_b(x_0, y_0, z_0, \theta, \phi)$, where b is the mirror index, as shown in Fig. 1(a). A reference frame, r , has its origin the point (x_0, y_0, z_0) and is inclined by (θ, ϕ) relative to the global reference

frame as illustrated in Fig. 1(b). The intersection between the mirrors is assumed to be located a long way from the extent of the incident beam and can therefore be neglected. To calculate the fields reflected and transmitted by a non-parallel FP etalon, we first construct a mirror-model to calculate the fields reflected and transmitted by a single mirror in isolation. This mirror-model is incorporated into a model of serially arranged individual optical components which takes into account all internal reflections within the FP cavity. The differing mirror orientations are accounted for by transforming the reference frame, in which the beam is described, into that of the mirror that the beam is incident upon.

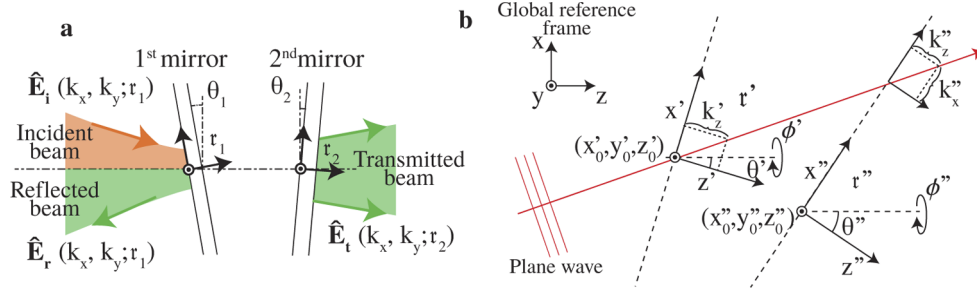


Fig. 1. a) Schematic diagram of light propagating in a non-parallel FP etalon. b) Schematic illustrating reference frame transformation for an angular spectrum.

2.1. Angular spectrum decomposition of fields

The fields transmitted and reflected by a mirror are easily computed if the field is described as an angular spectrum, i.e., as a sum of plane waves each having different complex amplitudes and directions of propagation [11]. However, to do this, the reference frame in which the incident field is defined must be the same as the mirror that light is incident upon. This is, however, not a problem since angular spectra can be transformed into an alternative reference frame with ease.

An angular spectrum, $\hat{\mathbf{E}}(k'_x, k'_y; \mathbf{r}')$, is calculated for a coordinate system which we define by a reference frame $\mathbf{r}'(x'_0, y'_0, z'_0, \theta'_0, \phi'_0)$, i.e., the plane wave with complex amplitude $\hat{\mathbf{E}}(k'_x, k'_y; \mathbf{r}')$ propagates with spatial directions (k'_x, k'_y, k'_z) defined on the coordinate system \mathbf{r}' and $\hat{\mathbf{E}}$ is the complex amplitude of the plane wave at the point (x'_0, y'_0, z'_0) (see Fig. 1(b)). An angular spectrum is given by the two-dimensional Fourier transform of the field in space as:

$$\hat{\mathbf{E}}(k'_x, k'_y; \mathbf{r}') = \int_{-\infty}^{\infty} \int_{-\infty}^{\infty} \mathbf{E}(x', y') \exp(i(k'_x x' + k'_y y')) dx' dy', \quad (1)$$

where (x', y') are the spatial coordinates in the $x - y$ plane of reference frame \mathbf{r}' , centered on the point (x'_0, y'_0, z'_0) as shown in Fig. 1(b) and $\mathbf{E}(x, y)$ is the field complex amplitude in space. The angular spectrum in an alternative reference frame $\mathbf{r}''(x''_0, y''_0, z''_0, \theta'', \phi'')$ may be calculated according to [12]:

$$\hat{\mathbf{E}}(k''_x, k''_y; \mathbf{r}'') = \mathcal{R}(\theta'') \mathcal{L}(\phi'') \mathcal{L}(-\phi') \mathcal{R}(-\theta') \hat{\mathbf{E}}(k'_x, k'_y; \mathbf{r}') \exp(i(k'_x \Delta x + k'_y \Delta y + k'_z \Delta z)), \quad (2)$$

where

$$k'_z = \pm \sqrt{k^2 - k_x^2 - k_y^2},$$

$$\begin{bmatrix} \Delta x \\ \Delta y \\ \Delta z \end{bmatrix} = \mathcal{R}(\theta') \mathcal{L}(\phi') \begin{bmatrix} x''_0 - x'_0 \\ y''_0 - y'_0 \\ z''_0 - z'_0 \end{bmatrix},$$

$$\begin{bmatrix} k''_x \\ k''_y \\ k''_z \end{bmatrix} = \mathcal{R}(\theta'') \mathcal{L}(\phi'') \mathcal{L}(-\phi') \mathcal{R}(-\theta') \begin{bmatrix} k'_x \\ k'_y \\ k'_z \end{bmatrix},$$

$$\mathcal{R}(\theta) = \begin{bmatrix} \cos(\theta) & -\sin(\theta) & 0 \\ \sin(\theta) & \cos(\theta) & 0 \\ 0 & 0 & 0 \end{bmatrix},$$

$$\mathcal{L}(\phi) = \begin{bmatrix} \cos(\phi) & 0 & \sin(\phi) \\ 0 & 0 & 0 \\ -\sin(\phi) & 0 & \cos(\phi) \end{bmatrix},$$

k is the wave number ($2\pi n/\lambda$), n the medium refractive index, λ the wavelength in vacuum, \mathcal{R} and \mathcal{L} are the rotation matrices relative to the y and z axes, respectively, and the sign of k'_z is chosen according to whether the field propagates in the positive- or negative- z direction, respectively. Eq. (2) is not valid for a field in an absorbing medium (i.e. if n is a complex number) or for evanescent waves [11] (i.e., if $k_x^2 + k_y^2 > k^2$). Under these conditions, transforming the angular spectrum reference frame requires the evaluation of two-dimensional Fourier and inverse Fourier transformations [12].

From this point onwards, we simplify the operation of changing the reference frame of a field by using the function $\mathfrak{C}(\mathbf{r}'', \mathbf{r}')$. The function $\mathfrak{C}(\mathbf{r}'', \mathbf{r}')$ transforms a field defined in the reference frame \mathbf{r}' into the same field but defined on the reference frame \mathbf{r}'' and is given by Eq. (2).

2.2. Reflected and transmitted fields by a mirror

Here we introduce the functions \mathfrak{R} and \mathfrak{T} , which relate an incident field with the fields reflected and transmitted by a mirror. Two different FP mirror representations are considered in this paper. In the first, the mirror is modelled as a layered medium comprising a series of layers of given complex refractive index and thickness. This solves Maxwell equations for the mirror dielectric structure but requires the precise mirror composition in terms of layers, refractive indices and thicknesses. In the second mirror representation, the mirror is modelled simply as a reflective interface of given spectrally varying reflectivity. This less rigorous approach is convenient when the full structure of the mirror is unknown or when it is simply desirable to think of the mirrors only in terms of their reflectivity.

If a mirror is defined as a layered refractive index distribution, \mathfrak{R} and \mathfrak{T} are given as:

$$\hat{\mathbf{E}}'_r(k_x, k_y; \mathbf{r}) = \mathfrak{R} \hat{\mathbf{E}}'(k_x, k_y; \mathbf{r}') = \mathfrak{R}' \mathfrak{C}(\mathbf{r}, \mathbf{r}') \hat{\mathbf{E}}'(k_x, k_y; \mathbf{r}'), \quad (3)$$

$$\hat{\mathbf{E}}'_t(k_x, k_y; \mathbf{r}) = \mathfrak{T} \hat{\mathbf{E}}'(k_x, k_y; \mathbf{r}') = \mathfrak{T}' \mathfrak{C}(\mathbf{r}, \mathbf{r}') \hat{\mathbf{E}}'(k_x, k_y; \mathbf{r}'), \quad (4)$$

where \mathfrak{R}' and \mathfrak{T}' are given by Eqs. (9) and (10) of [13] and \mathfrak{C} changes the field $\hat{\mathbf{E}}'$ reference frame \mathbf{r}' to the mirror reference frame \mathbf{r} . \mathbf{r} has its z -axis perpendicular to the mirror and its origin on

the mirror's first interface. The functions \mathfrak{R} and \mathfrak{T} are dependent on the direction of propagation of \mathbf{E}' .

For the case that the mirrors are described as an interface with reflectivity R and without light absorption, the functions \mathfrak{R} and \mathfrak{T} are given as:

$$\hat{\mathbf{E}}'_r(k_x, k_y; r) = \mathfrak{R} \hat{\mathbf{E}}'(k_x, k_y; r') = \pm \sqrt{R} \mathfrak{C}(r, r') \hat{\mathbf{E}}'(k_x, k_y; r') \quad (5)$$

$$\hat{\mathbf{E}}'_t(k_x, k_y; r) = \mathfrak{T} \hat{\mathbf{E}}'(k_x, k_y; r') = \frac{\sqrt[4]{(2\pi n_1/\lambda)^2 - k_x^2 - k_y^2}}{\sqrt[4]{(2\pi n_2/\lambda)^2 - k_x^2 - k_y^2}} \sqrt{1 - R} (\mathbf{N}_s(n_2)\mathbf{N}_s(n_1) + \mathbf{N}_p(n_2)\mathbf{N}_p(n_1)) \cdot \mathfrak{C}(r, r') \hat{\mathbf{E}}'(k_x, k_y; r'),$$

where \mathbf{N}_p and \mathbf{N}_s are the direction of light polarization defined as:

$$\mathbf{N}_p(n) = \begin{bmatrix} \frac{k_x k_z}{k_r k} & \frac{k_y k_z}{k_r k} & -\frac{k_r}{k} \end{bmatrix}^T, \quad (6)$$

$$\mathbf{N}_s(n) = \begin{bmatrix} \frac{k_y}{k_r} & \frac{-k_x}{k_r} & 0 \end{bmatrix}^T, \quad (7)$$

$$k_r = \sqrt{k_x^2 + k_y^2}, \quad (8)$$

$$k = \frac{2n\pi}{\lambda}, \quad (9)$$

and the choice of + or - on Eq. (5) depends on the direction of light propagation, n_1 and n_2 are the refractive index of the media before and after the reflective interface, respectively, and r is the reference frame defined on the reflective interface and with z axis perpendicular to it.

2.3. Reflected and transmitted fields by mirrors placed in series

The final stage of this model requires the iterative evaluation of the multiple partial reflections within the FP cavity as shown in Fig. 2(a). Following the notation introduced in Sec. 2.2, we use \mathfrak{R}_b and \mathfrak{T}_b to denote reflection and transmission of light by a mirror where b is the index of the mirror (i.e. first or second mirror). We further define $\mathfrak{R}_{1\leftrightarrow 2}$ and $\mathfrak{T}_{1\leftrightarrow 2}$ which relate the reflected, transmitted and incident fields for the combined structure formed by the mirrors with index 1 and 2. The functions $\mathfrak{R}_{1\leftrightarrow 2}$ and $\mathfrak{T}_{1\leftrightarrow 2}$ are calculated by summing all the partial fields generated between the two mirrors as shown in Fig. 2 and are given as:

$$\mathfrak{R}_{1\leftrightarrow 2} \hat{\mathbf{E}}_i = \mathfrak{R}_1 \hat{\mathbf{E}}_i + \sum_{j=0}^{\infty} \mathfrak{T}_1 (\mathfrak{R}_2 \mathfrak{R}_1)^j \mathfrak{R}_2 \mathfrak{T}_1 \hat{\mathbf{E}}_i, \quad (10)$$

$$\mathfrak{T}_{1\leftrightarrow 2} \hat{\mathbf{E}}_i = \sum_{j=0}^{\infty} \mathfrak{T}_2 (\mathfrak{R}_1 \mathfrak{R}_2)^j \mathfrak{T}_1 \hat{\mathbf{E}}_i, \quad (11)$$

where the j^{th} term of the sum is the partial field that makes j round trips in the FP cavity.

The calculation of the reflected and transmitted fields from a non-parallel FP etalon is concluded with Eqs. (10) and (11). For the sake of generality, we extend the model of non-parallel mirrors to allow for an arbitrary number, B , of non-parallel layered structures which can be used to simulate,

for example, non-parallel 3-mirror FP etalons [14]. Following the same rationale, $\mathcal{R}_{1\leftrightarrow 2}$ and $\mathcal{T}_{1\leftrightarrow 2}$ are generalized to an arbitrary number B as:

$$\mathcal{R}_{1\leftrightarrow b}\hat{\mathbf{E}}_i = \mathcal{R}_{1\leftrightarrow b-1}\hat{\mathbf{E}}_i + \sum_{j=0}^{\infty} \mathcal{T}_{1\leftrightarrow b-1}(\mathcal{R}_b \mathcal{R}_{1\leftrightarrow b-1})^j \mathcal{R}_b \mathcal{T}_{1\leftrightarrow b-1} \hat{\mathbf{E}}_i, \quad (12)$$

$$\mathcal{T}_{1\leftrightarrow b}\hat{\mathbf{E}}_i = \sum_{j=0}^{\infty} \mathcal{T}_b(\mathcal{R}_{1\leftrightarrow b-1} \mathcal{R}_b)^j \mathcal{T}_{1\leftrightarrow b-1} \hat{\mathbf{E}}_i. \quad (13)$$

To calculate $\mathcal{R}_{1\leftrightarrow B}$ and $\mathcal{T}_{1\leftrightarrow B}$, Eqs. (12) and (13) must be evaluated with b varying from 2 to B .

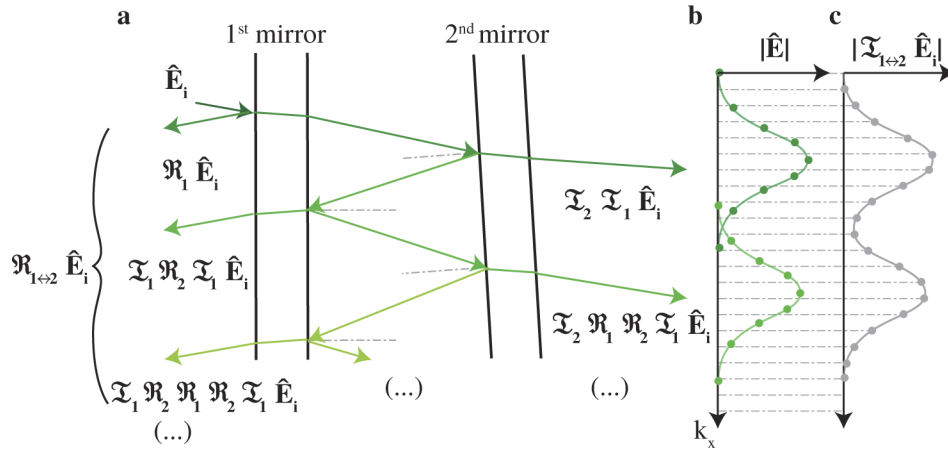


Fig. 2. a) Typical ray tracing diagram of two mirrors placed in series. b) Fields generated on each round trip inside the FP cavity defined on their respective sampling grid of (k_x, k_y) . The circles represent the sampling points and the lines the interpolated data. c) Sum of all fields generated on each round trip inside the cavity on the global grid (k_x, k_y) .

2.4. Numerical evaluation

The model described in Sec. 2.3 must be evaluated numerically. Our numerical evaluation samples an initial arbitrary angular spectrum, $\hat{\mathbf{E}}_i$, on a two-dimensional grid of (k_x, k_y) . The main challenge involved in the numerical implementation is that the grid points, upon which the angular spectrum is defined, change upon reflection by a mirror. This occurs for each partial reflection as illustrated in Fig. 2(b). In order to sum all round-trip terms, each must first be re-sampled onto a global grid of (k_x, k_y) . A solution, implemented in this paper, is to re-sample all such terms using a two-dimensional interpolation algorithm (such as bilinear interpolation) thus allowing the terms to be summed as illustrated in Fig. 2(c).

The model of non-parallel FP etalons sums of the infinite number of round trips made by light within the FP cavity. To approximate this infinite sum accurately, a sufficient number of terms must be summed such that the result converges. The number of rounds trips necessary to achieve convergence increases with the mirrors reflectivity. In our implementation the summation was truncated when the round trip intensity went below 10^{-8} of the initial field intensity. A single wavelength simulation runs typically in less than a minute on a standard desktop PC.

2.5. Model validation

Our model was validated using independent numerical models. As an initial validation, ITFs were computed for a parallel FP etalon with low-reflectivity mirrors using the model discussed in

this paper (by simulating two mirrors parallel to each other). This result was then compared with ITFs from a previously developed model of light propagation in parallel FP etalons [13]. ITFs from both models are shown in Fig. 3(a). As a second validation, the model was evaluated for an FP etalon with low reflectivity mirrors, this time forming an angle between them of 20 mrad. The resulting ITFs were compared against a model based on a numerical implementation of the Stratton-Chu integral [15,16]. The Stratton-Chu integral was evaluated iteratively to propagate the field between the mirrors (treated as reflective interfaces) in the non-parallel FP cavity [17]. All round trips were then summed to calculate the total transmitted beam. The ITFs from both models are shown in Fig. 3(b). The two results for the non-parallel mirror case do not agree perfectly since the Stratton-Chu based model is approximate. In particular, only a finite transverse area of the FP cavity is able to be sampled and some of the beam's energy will propagate outside of this sampled region. Furthermore, the Stratton-Chu integral is computationally intensive and so the spatial sampling has to be coarse ($\approx 2\lambda/3$) in order to run the simulations within days. Given the degree of approximation, we believe the agreement between the two models is good.

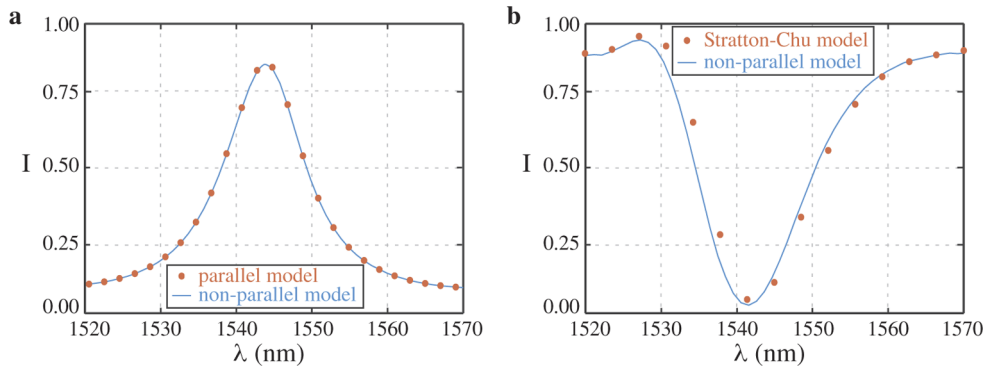


Fig. 3. Computed ITFs used to validate the non-parallel model with independent models.

3. Results

The model was used to perform a series of parametric studies to provide insight about the impact that an angle between the FP mirrors has on the ITF. In particular, over the expected range of design parameters including cavity thickness, mirror reflectivity and Gaussian illumination beam waist. In the following we consider a Gaussian beam with beam waist $2\omega_0$ (defined as the full width at $1/e^2$ of the intensity profile), normally incident and focused on the first mirror of an air spaced FP etalon, with cavity thickness h and mirrors represented by interfaces with reflectivity R . The second mirror is assumed to make an angle of α with respect to the first mirror. The wavelength range corresponds to that of the interferometer fringe nearest to 1500 nm. Transmissivity measurements were computed assuming a detector infinite in extent placed after the FP etalon, i.e. [18]:

$$I = k^2 \int_{-\infty}^{\infty} \int_{-\infty}^{\infty} |\hat{\mathbf{E}}(k_x, k_y)|^2 dk_x dk_y. \quad (14)$$

To allow for comparison between ITFs and plot trends as design parameters vary, we define the visibility (i.e. peak transmissivity) and the sensitivity as:

$$\text{visibility} = \max(I) \quad (15)$$

$$\text{sensitivity} \propto \max\left(\left|\frac{dI}{d\lambda}\right|\right), \quad (16)$$

where I is normalized to the incident beam intensity, i.e., the illumination beam has intensity one in that scale.

3.1. Varying cavity thickness

ITFs were computed for the angle the FP mirrors (α) varying between 0 mrad and 1.5 mrad and for cavity thickness (h) varying between 25 μm and 200 μm . A mirror reflectivity of 98 % and a Gaussian beam waist of 50 μm were assumed. The ITFs of parallel FP etalons plotted in Fig. 4 show that the ITFs broaden, become more asymmetric (with respect to wavelength), and experience reduced visibility as the cavity thickness increases. This behaviour has been explained on the basis of parallel FP etalons operating as angular-spectral filters when illuminated with focused beams [5]. Analysing the non-parallel cases, for a given cavity thickness, increasing the angle between FP mirrors leads to both visibility and asymmetry reducing and an increase in the Full Width Half Maximum (FWHM). This degradation of the ITF occurs because the tilted mirror induces a change in the propagation direction on every round trip (as represented in the schematic of Fig. 2). Due to the change in the direction of propagation, the phase change per round trip varies leading to a poorer interference between successive round trips.

Figure 4 also shows the visibility and sensitivity curves as a function of angle between FP mirrors for all cavity thicknesses considered. These plots show that both visibility and sensitivity decrease as the angle between FP mirrors increases. The impact of α on both visibility and sensitivity is largely independent of cavity thickness.

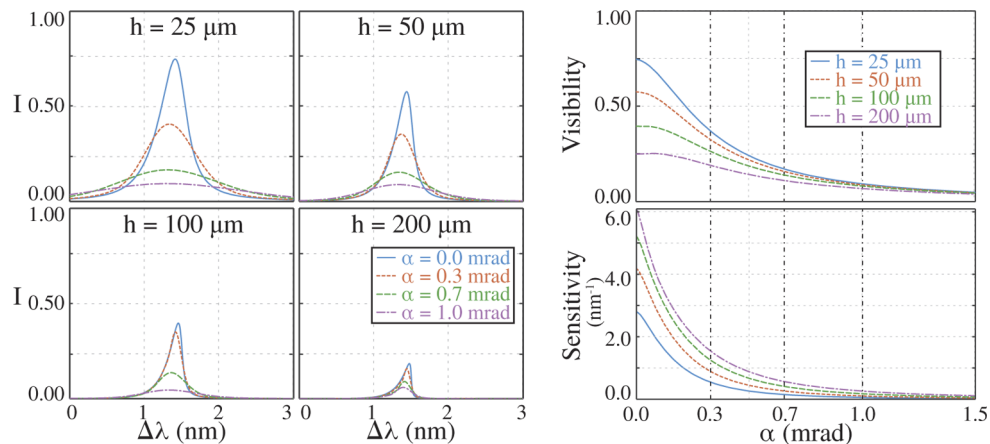


Fig. 4. Simulated ITFs and plots of visibility and sensitivity as a function of the angle between FP mirrors (α) and for different values of cavity thickness (h). A Gaussian beam waist of 50 μm and mirror reflectivities of 98% are assumed. All ITFs plots share the same legend. Both visibility and sensitivity plots share the same legend.

3.2. Varying mirror reflectivity

A series of ITFs were computed assuming a Gaussian beam waist of 50 μm , a cavity thickness of 100 μm and a mirror reflectivity (R) varying from 97 % to 99.5 %. The ITFs are plotted in Fig. 5. For parallel FP etalons an increase in the mirror reflectivity leads to a reduction in the visibility, an increase in the asymmetry, and an increase in the sensitivity. For all mirror reflectivities considered, an increase in the angle between FP mirrors leads to reduced visibility, increased FWHM and reduced asymmetry. Contrary to the case of varying cavity thickness, the impact of the angle between FP mirrors becomes more significant as the mirror reflectivity increases. This is demonstrated by the visibility and sensitivity plots which reduce more rapidly, with increasing

angle between FP mirrors, for high values of the mirror reflectivity. This is expected since, as the mirror reflectivity increases, the light undergoes more round trips inside the cavity, thus magnifying the impact of the non-parallelism.

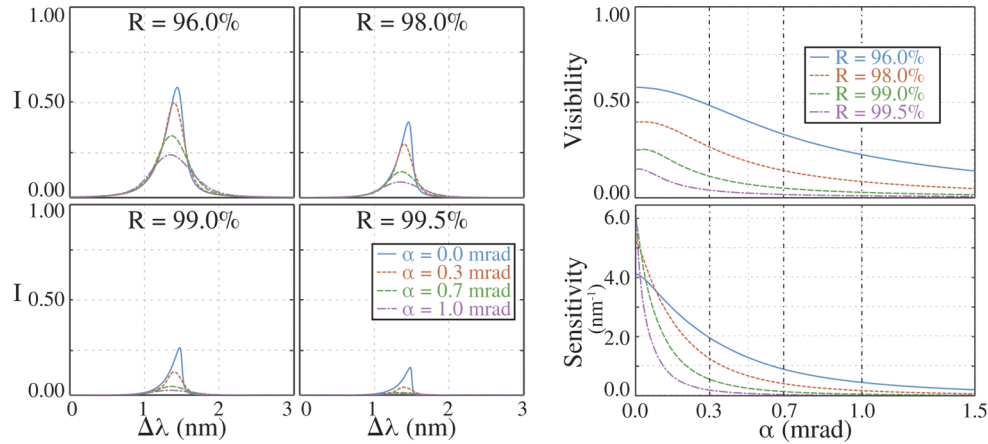


Fig. 5. Simulated ITFs and plots of visibility and sensitivity as function of the angle between FP mirrors (α) and for multiple values of mirror reflectivity (R). An air cavity 100 μm thick and a Gaussian beam waist of 50 μm are assumed. All ITFs plots share the same legend. Both visibility and sensitivity plots share the same legend.

3.3. Varying Gaussian beam waist

A series of ITFs were computed assuming a cavity 100 μm thick, mirror reflectivities of 98 % and Gaussian beam waist ($2\omega_0$) varying between 30 μm and 200 μm , which are plotted in Fig. 6. For parallel FP etalons, ITF visibility increases, whilst FWHM and asymmetry both decrease as the Gaussian beam waist increases. For all values of the Gaussian beam waist considered, an increase in the angle between FP mirrors leads to reduced visibility and increased FWHM. As the Gaussian beam waist increases, the impact of the angle between FP mirrors on the visibility and sensitivity becomes more significant, similar to the case of varying the mirror reflectivity. This is reasonable because a wider beam encounters a broader range of the cavity thicknesses, leading to a reduction in the sensitivity and visibility.

The parametric studies performed highlight some important considerations for the design of FP etalons with non-parallel mirrors. In particular, the significance of non-parallelism increases as the mirror reflectivity and the Gaussian beam waist increases, but is relatively insensitive to the cavity thickness. In applications where FP etalons are intended to be used as sensors, sensitivity is the most important characteristic. In general, mirror reflectivity is the primary FP sensor design variable, since the Gaussian beam waist defines the detection element size and the cavity thickness affects also the sensor response to the perturbation. For example, the cavity thickness and respective material defines the measurable ultrasound frequency range of an ultrasound FP sensor. In the case of ideal parallel FP etalons, the sensitivity is maximized with very high mirror reflectivity (> 99 %), irrespective of whether a collimated or focused Gaussian beam ($2\omega_0 > 30 \mu\text{m}$) is used [13]. However, these conclusions are not valid for non-parallel FP etalons, as shown by the modelled results. In particular, the sensitivity graph plotted in Fig. 5 shows that the optimal mirror reflectivity (that maximizes the sensitivity) depends on the angle between FP mirrors and, therefore, on the Gaussian beam waist as well.

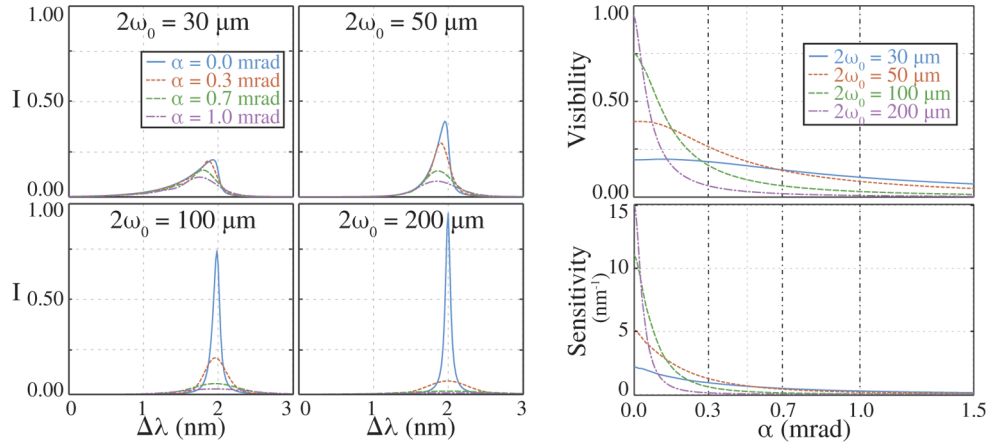


Fig. 6. Simulated ITFs and plots of visibility and sensitivity as a function of the angle between FP mirrors (α) and for multiple values of Gaussian beam waist ($2\omega_0$). An air cavity 100 μm thick and mirror reflectivities of 98% are assumed. All ITFs plots share the same legend. Both visibility and sensitivity plots share the same legend.

3.4. Tolerances on the angle between Fabry-Perot mirrors

Non-parallelism impacts negatively on both ITF visibility and sensitivity. Predicting the maximum allowable angle between FP mirrors, whilst still achieving high ITF visibility and sensitivity is difficult due to the complex relationships between the impact of non-parallelism and FP etalon design variables. To provide practical guidance on allowable angles between FP mirrors we have computed thresholds for the maximum angle between FP mirrors, as a function of mirror reflectivity (R), cavity optical path per wavelength (nh/λ , where n is the cavity refractive index) and Gaussian beam waist ($2\omega_0$). The maximum allowable angle between FP mirrors, α_{max} , is the angle between FP mirrors for which the sensitivity decreases to 95 % of the corresponding ideal parallel FP etalon, as the FP etalon design variables and illumination beam remain constant. The thresholds were computed for mirror reflectivity ranging from 90 % to 99.4 %, nh/λ ranging from 7 to 200 and Gaussian beam waist ranging from 30 μm to 300 μm . Example slices of the data cube are shown in Fig. 7.

The slices show that α_{max} is more dependent on the mirror reflectivity and Gaussian beam waist than cavity thickness. Furthermore, within the range of values considered in Fig. 7, the maximum allowable angle between FP mirrors varies by three orders of magnitude. This shows that the maximum tolerable angle is specific to a particular FP etalon and incident beam. For FP etalons with high mirror reflectivity, illuminated with a large Gaussian beam waist, the angle between FP etalons need to be below 1 μrad to result in high sensitivity ITFs. We have fitted a polynomial to the computed data to allow maximum angle between FP mirrors to be easily determined by the community for a specific combination of Gaussian beam waist, cavity optical path per wavelength and mirror reflectivities. The polynomial function is given as:

$$\alpha_{max}^{fit}(R, 2\omega_0, \frac{nh}{\lambda}) = -29.59 + 0.2577 \frac{nh}{\lambda} - \frac{22675}{2\omega_0} - \frac{46.56nh}{2\omega_0\lambda} - \frac{234696}{4\omega_0^2} + \frac{2275nh}{4\omega_0^2\lambda} + \frac{28.16}{R^2} - \frac{0.2437nh}{R^2\lambda} + \frac{23125}{R^2 2\omega_0} + \frac{44.29nh}{R^2 2\omega_0\lambda} + \frac{219528}{R^2 4\omega_0^2} - \frac{2342nh}{R^2 4\omega_0^2\lambda} \quad (17)$$

where $2\omega_0$ is defined in μm , R from 0.900 to 0.994 and α_{max}^{fit} in μrad . The error ϵ between the modelled data and the fit is $(7\pm 14)\%$ where ϵ is defined as:

$$\epsilon = \frac{|\alpha_{max}^{fit} - \alpha_{max}|}{\alpha_{max}}. \quad (18)$$

Equation (17) is empirical and obtained by fitting of the simulated data and should not be extrapolated beyond the range of simulated parameters. If the reader requires values outside the range considered, we recommend simulating the parameters required.

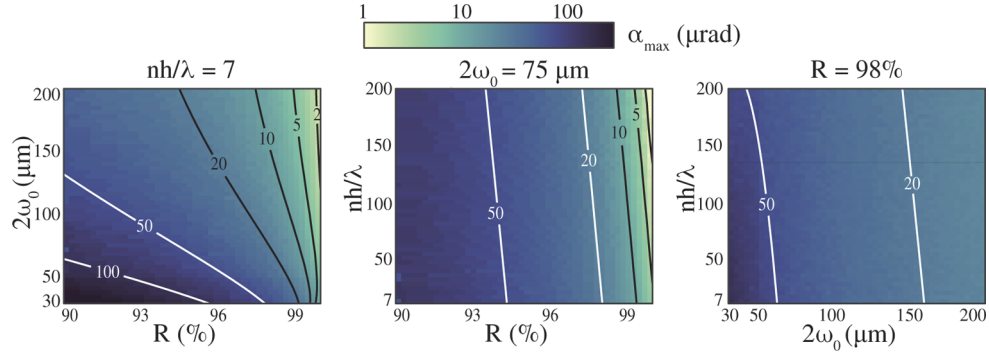


Fig. 7. Maximum allowable angle between FP mirrors (α_{max}) as a function of mirror reflectivities (R), cavity optical path per wavelength (nh/λ) and Gaussian beam waist ($2\omega_0$). α_{max} is defined as the angle between FP mirrors which reduces the sensitivity of the ITF to 95 % of the corresponding parallel case. The isolines plotted are calculated from α_{max}^{fit} .

4. Conclusion

We have presented a full wave model for calculating the propagation of arbitrary optical fields inside non-parallel FP etalons. The model was applied to study the impact of having a small angle between the mirrors of an FP etalon on its ITF. Specifically, a range of parametric studies were performed in which the angle between mirrors was varied. These studies were carried out for FP etalons with different mirror reflectivities, cavity thicknesses and illumination Gaussian beam waists. These simulations were used to quantify the impact of non-parallelism on visibility and sensitivity. For all conditions simulated, an angle between FP mirrors degrades the ITF and, in particular, it reduces the visibility and sensitivity. That reduction in visibility and sensitivity increases with the mirror reflectivity and the Gaussian beam waist but is almost independent of the cavity thickness. Furthermore, we concluded that the design that optimizes the visibility and/or sensitivity of an FP etalon depends on the angle between the FP etalon and must therefore be considered. Finally, an empirically derived polynomial was presented to provide a guideline on the maximum allowable angle between FP mirrors whilst maintaining high visibility and high sensitivity. The results show that this maximum allowable angle is strongly dependent on the mirror reflectivity and the incident Gaussian beam waist, as demonstrated by its variation over three orders of magnitude.

Our model could aid the design and understanding of optical systems involving non-parallel FP etalons. Such systems include photoacoustic imaging systems based on polymer film FP etalons [19] for which the ITF cannot be predicted with parallel FP etalon models [8]. In particular, by assuming a particular angle between FP mirrors, cavity thickness and incident Gaussian beam waist, the model can be used to calculate the optimal mirror reflectivity to maximise the optical sensitivity of the FP ultrasound sensor. Beyond modelling the non-parallel cavity of an FP etalon,

the model could also be used to calculate the effect of non-parallel optical layers external to the FP etalon. For example, FP ultrasound sensors are typically built on a wedged substrate [19]. This substrate provides physical support to the sensor, while its wedged shape enables avoiding any parasitic interference. By including the wedged substrate in addition to the FP etalon itself, our model could be used to calculate the beam aberrations induced by the wedged substrate and its effect upon the ITF and sensor sensitivity.

Funding. Royal Society (URF\R\191036, URF\R1\180435); European Research Council (741149); EPSRC Centre for Doctoral Training in Medical Imaging (EP/L016478/1).

Disclosures. The authors do not declare any financial interests or conflicts of interest.

Data availability. The data and code underlying the results presented in this paper may be obtained upon reasonable request.

References

1. A. Perot and C. Fabry, "On the application of interference phenomena to the solution of various problems of spectroscopy and metrology," *The Astrophys. J.* **9**, 87 (1899).
2. M. Vaughan, *The Fabry-Perot interferometer: history, theory, practice and applications* (Routledge, 2017).
3. S. Irmer, J. Daleiden, V. Rangelov, C. Prott, F. Römer, M. Strassner, A. Tarraf, and H. Hillmer, "Ultralow biased widely continuously tunable Fabry-Pérot filter," *IEEE Photonics Technol. Lett.* **15**(3), 434–436 (2003).
4. E. Zhang and P. Beard, "Broadband ultrasound field mapping system using a wavelength tuned, optically scanned focused laser beam to address a Fabry Perot polymer film sensor," *IEEE Trans. Ultrason., Ferroelect., Freq. Contr.* **53**(7), 1330–1338 (2006).
5. J. Y. Lee, J. W. Hahn, and H.-W. Lee, "Spatiospectral transmission of a plane-mirror Fabry-Perot interferometer with nonuniform finite-size diffraction beam illuminations," *J. Opt. Soc. Am. A* **19**(5), 973 (2002).
6. A. P. Jathoul, J. Laufer, O. Ogunlade, B. Treeby, B. Cox, E. Zhang, P. Johnson, A. R. Pizzey, B. Philip, T. Marafioti, M. F. Lythgoe, R. B. Pedley, M. A. Pule, and P. Beard, "Deep in vivo photoacoustic imaging of mammalian tissues using a tyrosinase-based genetic reporter," *Nat. Photonics* **9**(4), 239–246 (2015).
7. D. R. Ramasawmy, "Modelling the Directional Response of Fabry-Pérot Ultrasound Sensors," Ph.D. thesis, University College London (2020).
8. D. Marques, J. A. Guggenheim, R. Ansari, E. Z. Zhang, P. C. Beard, and P. R. T. Munro, "Flatness of planar Fabry-Pérot cavities: a critical parameter for high sensitivity sensors for photoacoustic imaging (Conference Presentation)," in *Photons Plus Ultrasound: Imaging and Sensing 2020*, A. A. Oraevsky and L. V. Wang, eds. (SPIE, 2020), p. 30.
9. G. Xia, Z. Wu, M. Liu, and Y. Pan, "Transmitted characteristics for a Gaussian beam passing through a misaligned Fabry-Perot interferometer," *Optik* **114**(12), 521–524 (2003).
10. O. J. Sheppard, J. A. Guggenheim, D. M. Marques, R. Ansari, E. Z. Zhang, P. C. Beard, and P. R. T. Munro, "Interrogation of Fabry-Pérot ultrasound sensors with Bessel beams," in *Photons Plus Ultrasound: Imaging and Sensing 2020*, A. A. Oraevsky and L. V. Wang, eds. (SPIE, 2020), p. 39.
11. L. Novotny and B. Hecht, *Principles of nano-optics* (Cambridge University, 2012).
12. N. Delen and B. Hooker, "Free-space beam propagation between arbitrarily oriented planes based on full diffraction theory: a fast Fourier transform approach," *J. Opt. Soc. Am. A* **15**(4), 857 (1998).
13. D. M. Marques, J. A. Guggenheim, R. Ansari, E. Z. Zhang, P. C. Beard, and P. R. T. Munro, "Modelling Fabry-Pérot etalons illuminated by focussed beams," *Opt. Express* **28**(5), 7691 (2020).
14. M. Stephen, M. Fahey, and I. Miller, "Solid, 3-mirror Fabry-Pérot etalon," *Appl. Opt.* **56**(10), 2636 (2017).
15. J. A. Stratton and L. J. Chu, "Diffraction theory of electromagnetic waves," *Phys. Rev.* **56**(1), 99–107 (1939).
16. P. Török, P. R. Munro, and E. E. Kriezis, "Rigorous near- to far-field transformation for vectorial diffraction calculations and its numerical implementation," *J. Opt. Soc. Am. A* **23**(3), 713 (2006).
17. H. Varu, "The optical modelling and design of Fabry Perot Interferometer sensors for ultrasound detection," Ph.D. thesis, University College London (2014).
18. C. Sheppard and A. Choudhury, "Image Formation in the Scanning Microscope," *Opt. Acta* **24**(10), 1051–1073 (1977).
19. E. Zhang, J. Laufer, and P. Beard, "Backward-mode multiwavelength photoacoustic scanner using a planar Fabry-Perot polymer film ultrasound sensor for high-resolution three-dimensional imaging of biological tissues," *Appl. Opt.* **47**(4), 561 (2008).